



Cite as  
Nano-Micro Lett.  
(2021) 13:2

Received: 30 June 2020  
Accepted: 28 August 2020  
© The Author(s) 2020

## Superior Pseudocapacitive Storage of a Novel $\text{Ni}_3\text{Si}_2/\text{NiOOH}/\text{Graphene}$ Nanostructure for an All-Solid-State Supercapacitor

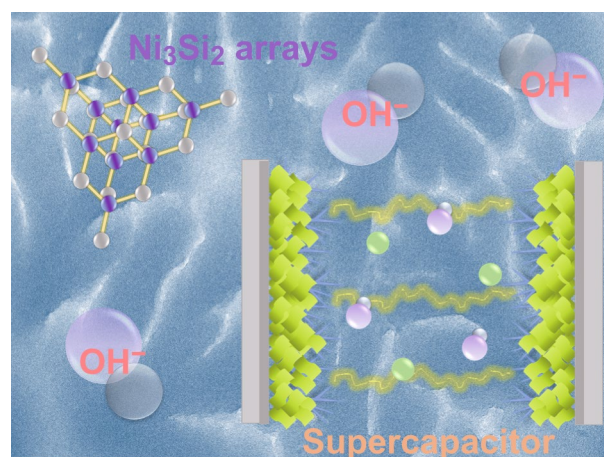
Jing Ning<sup>1,2</sup> ✉, Maoyang Xia<sup>1,2</sup>, Dong Wang<sup>1,2</sup> ✉, Xin Feng<sup>1,2</sup>, Hong Zhou<sup>1,2</sup>,  
Jincheng Zhang<sup>1,2</sup>, Yue Hao<sup>1,2</sup>

### HIGHLIGHTS

- Three types of  $\text{Ni}_3\text{Si}_2$  were successfully fabricated by low-pressure all-solid melting-reconstruction chemical vapor deposition, and the growth pattern changed with the carbon source content.
- In a carbon-rich atmosphere, high-energy atoms bombard the Ni and Si surface, and reduce the free energy in the solid Ni–Si particles' thermodynamic equilibrium, considerably catalyzing the growth of Ni–Si nanocrystals.
- $\text{Ni}_3\text{Si}_2/\text{NiOOH}/\text{graphene}$  provides a large specific area and NiOOH inhibits insulation on the electrode surface in an alkaline solution and accelerates the electron exchange rate.

**ABSTRACT** Recent developments in the synthesis of graphene-based structures focus on continuous improvement of porous nanostructures, doping of thin films, and mechanisms for the construction of three-dimensional architectures. Herein, we synthesize creeper-like  $\text{Ni}_3\text{Si}_2/\text{NiOOH}/\text{graphene}$  nanostructures via low-pressure all-solid melting-reconstruction chemical vapor deposition. In a carbon-rich atmosphere, high-energy atoms bombard the Ni and Si surface, and reduce the free energy in the thermodynamic equilibrium of solid Ni–Si particles, considerably catalyzing the growth of Ni–Si nanocrystals. By controlling the carbon source content, a  $\text{Ni}_3\text{Si}_2$  single crystal with high crystallinity and good homogeneity is stably synthesized. Electrochemical measurements indicate that the nanostructures exhibit an ultrahigh specific capacity of  $835.3 \text{ C g}^{-1}$  ( $1193.28 \text{ F g}^{-1}$ ) at  $1 \text{ A g}^{-1}$ ; when integrated as an all-solid-state supercapacitor, it provides a remarkable energy density as high as  $25.9 \text{ Wh kg}^{-1}$  at  $750 \text{ W kg}^{-1}$ , which can be attributed to the free-standing  $\text{Ni}_3\text{Si}_2/\text{graphene}$  skeleton providing a large specific area and NiOOH inhibits insulation on the electrode surface in an alkaline solution, thereby accelerating the electron exchange rate. The growth of the high-performance composite nanostructure is simple and controllable, enabling the large-scale production and application of microenergy storage devices.

**KEYWORDS** Pseudocapacitive storage; Creeper-like  $\text{Ni}_3\text{Si}_2$ ; NiOOH; Graphene; All-solid-state supercapacitors



✉ Jing Ning, [ningj@xidian.edu.cn](mailto:ningj@xidian.edu.cn); Dong Wang, [chankwang@xidian.edu.cn](mailto:chankwang@xidian.edu.cn)

<sup>1</sup> The State Key Discipline Laboratory of Wide Band Gap Semiconductor Technology, Xidian University, Xi'an 710071, People's Republic of China

<sup>2</sup> Shaanxi Joint Key Laboratory of Graphene, Xidian University, Xi'an 710071, People's Republic of China



## 1 Introduction

Electrical energy storage systems have become one of the key research objects that are studied to address current energy challenges such as the rapid consumption of fossil fuels, environmental pollution, and global warming [1, 2]. Rechargeable energy storage devices, including traditional capacitors, supercapacitors (SCs), batteries, and fuel cells, are widely used in consumer electronics, transportation, and renewable energy fields [3]. SCs, also called double-layer capacitors, have attracted widespread attention owing to their advantages such as high reliability, fast charge–discharge speed, and high-safety performance [4]. SCs can be classified as: electrical double-layer capacitors and pseudocapacitors [5]. Electrical double-layer capacitor materials, such as three-dimensional (3D) graphene, which have good electrical conductivity and large specific surface area, adsorb electrolyte ions on their surface to store energy [6, 7]. However, the agglomeration and collapse of the 3D structure during operation affect device performance because of the decreased specific surface area [8, 9]. The most effective method to solve this problem is to develop an alternative anode material with a novel structure.

During the nanotechnology revolution of recent decades, one-dimensional nanostructures, such as nanowires, nanotubes, and nanorods, have attracted widespread attention because of their unique physical and chemical properties [10]. The preparation of various nanostructures has significantly progressed using nickel sulfide, which is one of the electrode materials used for lithium batteries [11]. Examples include porous NiS nanoflake arrays [12], Ni<sub>3</sub>S<sub>2</sub> and Co<sub>9</sub>S<sub>8</sub> double-size nanoparticles [13], hierarchically structured Ni<sub>3</sub>S<sub>2</sub>/carbon nanotubes [14], Ni<sub>3</sub>S<sub>2</sub>@MoS<sub>2</sub> core shell nanorods on Ni foam [15], NiS<sub>2</sub> nanocubes [16], Ni<sub>3</sub>S<sub>2</sub>@Ni composites [17], and Ni<sub>3</sub>S<sub>2</sub> nanorod arrays on Ni–graphene foams [18]. However, NiS<sub>2</sub> electrodes have several disadvantages, such as low capacity, poor cycle life, large volume change rate, and solubility in electrolytes, limiting their use in supercapacitors [19]. For example, Pang et al. [16] reported that a NiS<sub>2</sub> nanocube prepared via the microwave-assisted method has good cycle stability (maintaining 93.4% of the initial specific capacitance after 3000 cycles). However, the specific capacitance of the NiS<sub>2</sub> nanocube is poor (695 F g<sup>-1</sup>, 1.25 A g<sup>-1</sup>). Wang et al. [20] highlighted that internal stress, which gradually

increases as the reaction during the ion insertion/extraction process progresses, cracks, and pulverizes the transition metal sulfide particles. The irreversibility of the electrode material's microstructural evolution causes the electrode to generate a large irreversible capacity loss in the first cycle. Problems, such as slow ion diffusion and low mobility at the solid–liquid interface, further degrade the performance of the NiS electrode. The most advantageous strategies to solve the above-mentioned problems, including buffering large volume changes of electrodes and improving conductivity, involve the engineering of new nanostructures and the controlled synthesis of new Ni compounds.

Compared with other electrode materials, nickel silicide is advantageous because of its large mechanical stress tolerance, good electrical conductivity, and high electrochemical performance. It is a potential candidate material for supercapacitor electrodes. More importantly, its growth is compatible with and can be easily integrated into silicon process technology [21, 22]. Accordingly, Nickel silicide nanostructures provide a very large surface area because of their unique network structure. In addition, nickel silicide used in binder-free electrodes (the material can be directly grown on a conductive substrate) forms an excellent interface with nickel and exhibits low internal resistance [7]. Jiang et al. [7] reported that Ni<sub>3</sub>Si<sub>2</sub> nanowires prepared via low-pressure chemical vapor deposition have a high specific capacitance (760 F g<sup>-1</sup> at 0.5 A g<sup>-1</sup>) and low series resistance (0.93 Ω). By definition, high specific capacitance and low series resistance are key factors to mitigating the tradeoff between the power and energy densities. Therefore, nickel silicide can be used as a new electrode material to solve the limitations of traditional electrical double-layer capacitor materials in supercapacitor applications.

Herein, we synthesized novel creeper-like Ni<sub>3</sub>Si<sub>2</sub>/graphene using a simple and effective low-pressure all-solid melting-reconstruction chemical vapor deposition (LSRCVD) method. The Ni<sub>3</sub>Si<sub>2</sub>/NiOOH/graphene composite nanostructures were synthesized through a hydrothermal method. Based on systematic micromorphological characterization, the formation mechanism of the nanostructures is discussed to develop reliable and controllable nanostructure preparation technology. Under bombardment by high-energy particles in a carbon-rich environment, supersaturation of the Si precursor is decreased by using Ni as the substrate. The silicon vapor is cooled and crystallized on

a molten nickel substrate to form Ni–Si nanostructures. By adjusting the carbon content and growth time, we successfully achieved  $\text{Ni}_3\text{Si}_2$  nanocrystal growth in the axial direction and fabricated nanostructures with high surface areas under Ar gas etching. The electrochemical test confirms that the  $\text{Ni}_3\text{Si}_2/\text{NiOOH}/\text{graphene}$  composite exhibits extremely good performance. The specific capacitance of the  $\text{Ni}_3\text{Si}_2/\text{NiOOH}/\text{graphene}$  electrode reaches  $835.3 \text{ C g}^{-1}$  ( $1193.28 \text{ F g}^{-1}$ ) at  $1 \text{ A g}^{-1}$ . The fabricated all-solid-state supercapacitor exhibits a maximum energy density of  $25.9 \text{ Wh kg}^{-1}$  at  $750 \text{ W kg}^{-1}$ . These properties are due to the following reasons: First, the  $\text{Ni}_3\text{Si}_2/\text{graphene}$  nanoskeleton possesses excellent mechanical strength and supports the entire electrode. Simultaneously,  $\text{Ni}_3\text{Si}_2$  effectively guides the directional deposition of NiOOH with high crystal quality. NiOOH inhibits the insulation of the electrode surface in an alkaline solution and accelerates the electron exchange rate. Second, the interconnected nanostructures have large specific surface areas. Even if parts of the nanoflakes are disconnected from the substrate, the internal electronic circulation will still be protected by physical contact with adjacent nanostructures. Third, in a carbon-rich atmosphere, the surface free energy of solid Ni–Si particles in a thermodynamic equilibrium decreases and excess Ni rapidly diffuses into Ni–Si nanoparticles, which facilitates the formation of Ni–Si nanostructures. Nanoparticles grow in the radial direction to form creeper-like nanostructures. The creeper-like structure increases the specific surface area of the electrode material and the active sites, thereby inducing more redox reactions in the nickel substrate in addition to high conductivity, generating fast charge-transfer kinetics and thus better performance. Fourth, because of the self-supporting 3D porous nanostructure, electrons can traverse the entire electrode surface, creating a convenient electron transfer path for active nanomaterials, thereby improving the supercapacitor performance. The excellent electrochemical properties indicate the potential for integrated SC applications and marketization.

## 2 Experimental Section

### 2.1 Fabrication of Nanostructures

The creeper-like nanostructures were grown on commercial Ni foam in three steps. First, a hybrid  $\text{Ni}_3\text{Si}_2/\text{graphene}$

structure was fabricated using a laboratory-made low-pressure chemical vapor deposition (CVD) system. Initially, the surface of the Ni foam was sonicated in a  $0.3 \text{ mol L}^{-1}$   $(\text{NH}_4)_2\text{S}_2\text{O}_8$  solution for 5 min to remove contaminants and oxides. After washing with analytical-grade acetone, ethanol, and deionized water for 5 min each, the Ni foam was dried with nitrogen. Next, the cleaned Ni foam/Si (111) stack was placed into the quartz tube furnace of the CVD system at a base vacuum of  $\sim 0.1 \text{ Pa}$ . Ultrahigh-purity hydrogen was injected into the furnace tube at a flow rate of 10 sccm. Subsequently, the nickel foam was heated from 30 to  $1030 \text{ }^\circ\text{C}$  at a heating rate of  $20 \text{ }^\circ\text{C min}^{-1}$ . Once the temperature reached  $1030 \text{ }^\circ\text{C}$ , ultrahigh-purity methane was introduced into the furnace tube (flow rate of 50 sccm) as the carbon source for 2 h. Second, the sample was cooled to  $1000 \text{ }^\circ\text{C}$  and annealed for 1 h in a mixed atmosphere (10 sccm hydrogen, 50 sccm methane and 800 sccm argon). The tube was then slowly cooled to ambient temperature at a cooling rate of  $\sim 5 \text{ }^\circ\text{C min}^{-1}$  under 10 sccm of hydrogen flow. Third, the  $\text{Ni}_3\text{Si}_2/\text{NiOOH}/\text{graphene}$  nanostructure was synthesized using a hydrothermal method. The metal foams were selectively etched in a mixture of 1 M  $\text{FeCl}_3$  and 2 M HCl at  $60 \text{ }^\circ\text{C}$  overnight and free-standing  $\text{Ni}_3\text{Si}_2/\text{graphene}$  was obtained. Subsequently, 100 mg urea was uniformly dispersed in 40 mL deionized water by stirring for 1 h. The mixture was then transferred into a 60-mL Teflon-lined stainless-steel autoclave and the fabricated  $\text{Ni}_3\text{Si}_2/\text{graphene}$  was added to the mixture. The autoclave was subsequently sealed and maintained at  $180 \text{ }^\circ\text{C}$  for 2 h. Once the reaction was completed, the autoclave was cooled to room temperature. Finally, the sample was clamped with tweezers and washed three times with deionized water and ethanol. The final product was obtained after drying overnight under vacuum at  $80 \text{ }^\circ\text{C}$ . The mass of the graphene,  $\text{Ni}_3\text{Si}_2$ , and NiOOH are about 0.18, 0.26, and 0.26 mg, respectively. The detailed analysis process is in the supporting information.

The synthesis process of NiOOH/graphene and  $\text{Ni}_3\text{Si}_2/\text{graphene}$  is similar to that of  $\text{Ni}_3\text{Si}_2/\text{NiOOH}/\text{graphene}$ , and the detailed process is in the supporting information.

### 2.2 Nanostructure Characterization

The morphologies of the  $\text{Ni}_3\text{Si}_2/\text{NiOOH}/\text{graphene}$  nanostructures were investigated via scanning electron microscopy (SEM) (Quanta 600FEG, FEI, USA). The crystallinity



of the materials was evaluated through high-resolution X-ray diffraction (XRD) (D8 Discovery, Bruker, Germany) in Bragg (reflection) geometry and Cu  $K_{\alpha 1}$  radiation (wavelength:  $\lambda = 1.54056 \text{ \AA}$ ). The Raman spectrum was obtained with a Raman spectroscopy system (LabRam HR 800, Horiba JY, Japan) using an  $\text{Ar}^+$  laser (514 nm wavelength) as the excitation source. The elemental analyses of the composites were conducted via X-ray photoelectron spectroscopy (XPS) (ESCALAB, 250Xi, Thermo Fisher Scientific, USA).

### 2.3 Supercapacitor Fabrication and Evaluation

Cyclic voltammetry (CV), galvanostatic charge/discharge (GCD), and electrochemical impedance spectroscopy (EIS) were performed using the CHI660 electrochemical workstation and a three-electrode test system including the active material as the working electrode,  $\text{Ag}/\text{AgCl}$  as the reference electrode, platinum mesh as the counter-electrode, and 3 M KOH as the electrolyte.

Based on the GCD curves, the specific capacity  $Q_s$  ( $\text{C g}^{-1}$ ) and specific capacitance  $C_g$  ( $\text{F g}^{-1}$ ) can be computed using Eqs. (1) and (2):

$$Q_s = \frac{I\Delta t}{m} \quad (1)$$

$$C_g = \frac{I\Delta t}{m\Delta V} \quad (2)$$

where  $I$  is the discharge current (A),  $m$  is the total weight (g) and  $\Delta t$  is the discharge time (s).

All SC cell electrochemical measurements were performed using the prepared “sandwich” capacitor. The electrodes, cellulose diaphragms, and electrodes were stacked, and the active materials were in direct contact with the current collector. The electrolyte was gelatinous PVA-KOH.

The specific capacitance ( $C_g$ ) of the SC cell was calculated using the GCD curves and Eq. (4). The energy and power densities of the SC cell were obtained from Eqs. (3) and (4):

$$E = \frac{1}{2} C_g \Delta V^2 \quad (3)$$

$$P = \frac{E}{\Delta t} \quad (4)$$

where  $E$  is the energy density ( $\text{Wh kg}^{-1}$ ) and  $P$  is the power density ( $\text{W kg}^{-1}$ ).

## 3 Results and Discussion

### 3.1 Characterizations

To ensure high purity and controllability, novel creeper-like  $\text{Ni}_3\text{Si}_2/\text{NiOOH}/\text{graphene}$  nanostructures were synthesized on 3D graphene/Ni foam using a three-step method. Figure 1 schematically illustrates the formation mechanism of the creeper-like  $\text{Ni}_3\text{Si}_2/\text{NiOOH}/\text{graphene}$  nanostructures.

In the first step,  $\text{CH}_4$  was decomposed through catalysis with the Ni foam and the carbon atoms dissolved in the 3D Ni foam. Simultaneously, the Si vapor mixed with Ni vapor in a carbon-rich environment, the formation of Ni–Si nanocores form from supersaturation of Ni/Si vapor, the nanocore melting, cooled and then condensed on the surface of the Ni foam. Several Ni–Si nanocores formed during condensation. In the second step, carbon atoms precipitated from the Ni foam and were transferred into graphene along the 3D Ni foam surface during annealing. During melting and condensation, the Ni–Si nuclei randomly merged and flowed on the graphene surface. Then, these nuclei grew radially and axially, forming a creeper-like nanoskeleton. In the third step, several  $\text{Ni}_3\text{Si}_2$  units on the surface reacted with urea during the hydrothermal process to form NiOOH nanosheets, which dissolved in the solution.  $\text{Ni}_3\text{Si}_2$  acts as the nanoframework to guide the deposition of NiOOH nanosheets, and a creeper-like nanostructure forms through the complex directional adhesion process.

The carbon content is one of the main factors affecting the synthesis of  $\text{Ni}_3\text{Si}_2$  nanostructures using LSRCVD. The way to control the carbon content is to change the Ar flow rate. In the experiment, 12.5% carbon content atmosphere includes 10 sccm  $\text{H}_2$ , 50 sccm  $\text{CH}_4$ , 340 sccm Ar, 6.25% carbon content atmosphere includes 10 sccm  $\text{H}_2$ , 50 sccm  $\text{CH}_4$ , 740 sccm Ar, and 4.17% carbon content atmosphere includes 10 sccm  $\text{H}_2$ , 50 sccm  $\text{CH}_4$ , 1140 sccm Ar. During annealing, Ni–Si nanocrystals start to grow; the gas flow rate strongly affects the growth of the nanostructures, as shown in Fig. 2. After high-temperature heating, a large amount of irregular Ni–Si dust (average size of  $\sim 6000 \text{ nm}^2$ ) condensed and crystallized as the crystal nucleus on the surface of the Ni foam (Fig. 2a). In the carbon-rich environment (carbon content > 10%), the  $\text{Ni}_3\text{Si}_2$  nanostructure followed a radial growth model (Fig. 2b). In the radial direction, a small amount of Si vapor condensed owing to the large amount of

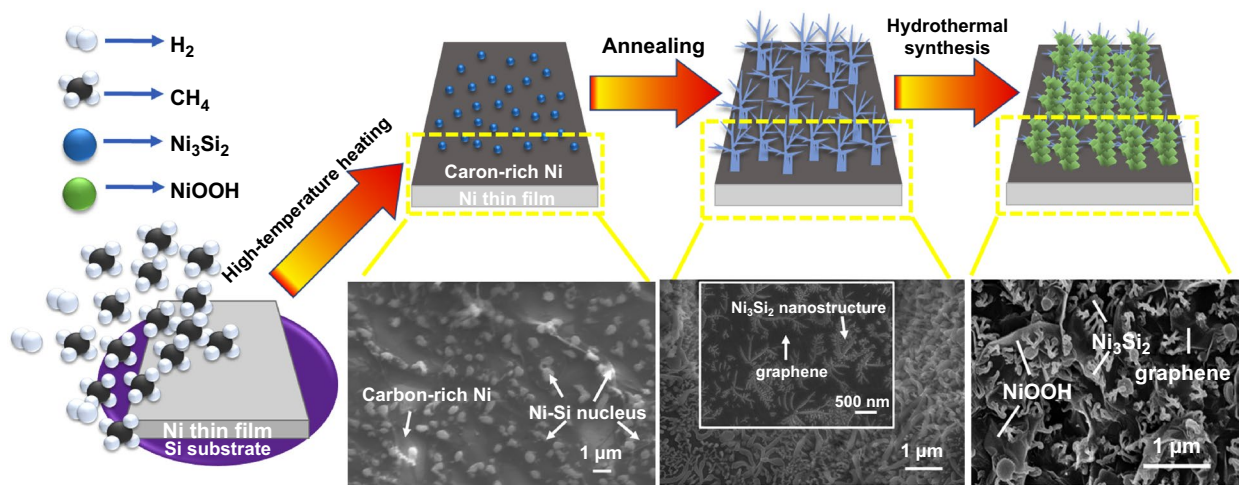


**Fig. 1** Schematic diagram of the formation and evolution of creeper-like nanostructures

$\text{CH}_4$ , the supersaturation of Ni vapor was high, and the surface free energy of the Ni–Si core in thermodynamic equilibrium was reduced. Thermally activated Ni atoms continuously and rapidly diffused to the Ni–Si nucleation center and reached a certain degree of supersaturation, resulting in the growth of columnar roots in the Ni–Si nanocrystals. With decreasing carbon content ( $\sim 10\%$ ), the crystallization mechanism changed to predominant axial growth (Fig. 2c). The variation of the surface free energy becomes small because of the decrease in Si and Ni vapor saturation, rendering the radial diffusion of Ni atoms difficult. The Ni–Si dust melted into droplets and subsequently coalesced. Ni–Si droplets with long tails formed in different directions on the surface of the Ni foam. At a very low carbon content ( $< 5\%$ ), the radial growth of Ni–Si nanostructures was completely inhibited. The evaporated Si and Ni were quickly removed by Ar. The thin film on the surface relied on the combination of Ni–Si dust and a porous structure formed under the etching of Ar (Fig. 2d). Figure 2e, f shows the effects of the carbon content on the morphology, size, and density of the  $\text{Ni}_3\text{Si}_2$  crystals. With reduction in the carbon content, the crystal morphology changed from nanowire- to creeper-shaped, and the crystals finally became amorphous (SEM, TEM and EDS images of amorphous  $\text{Ni}_3\text{Si}_2$  are shown in Fig. S2). Because decreased number of carbon atoms increased the required surface free energy, Ni–Si nucleation became difficult. Figure 2f shows that the density and size reached extreme values at a carbon content of 6.25%. The largest specific area is observed under these conditions. These results

demonstrate the validity of the above-mentioned nucleation theory. Therefore, carbon regulation can be used to control the morphology, size, and density of crystals.

The annealing time is another key factor affecting the fabrication of  $\text{Ni}_3\text{Si}_2$  nanostructures using LSRCVD. Figure 3 shows SEM images of the  $\text{Ni}_3\text{Si}_2$  nanostructures for different growth times with 6.25% carbon content. Initially, mostly incomplete nanostructures were formed. In addition, the densities of the nanostructures were low, as shown in Fig. 3a. With the increase in the annealing time from 0 to 30 min, the densities and average sizes of the creeper-like nanostructures gradually increased. After 30 min, the densities of the creeper-like nanostructures decreased; however, the average sizes continued to increase (Fig. 3b, c). At the beginning of annealing, the Ni–Si content was low. The Ni and Si vapors continuously condensed on the Ni surface, producing enough nuclei and growth. With increasing nuclear density, the space for nanostructure nucleation decreased, and several nanoflakes merged to form large-scale nanostructures. However, the growth mechanism controlled by the diffusion of the solid phase requires a specific particle size range, which limits the nanostructure size. Therefore, the average size and nuclear density appear to be competitive, which provides the possibility of controlled  $\text{Ni}_3\text{Si}_2$  nanostructure growth.

Figure 4 shows the TEM (inset: schematic structures of  $\text{Ni}_3\text{Si}_2/\text{NiOOH}/\text{graphene}$ ) and EDS images of the  $\text{Ni}_3\text{Si}_2/\text{NiOOH}/\text{graphene}$  creeper-like nanostructures. The lattice fringe distances of 0.25, 0.32, 0.33, and 0.46 nm in Fig. 4b–d

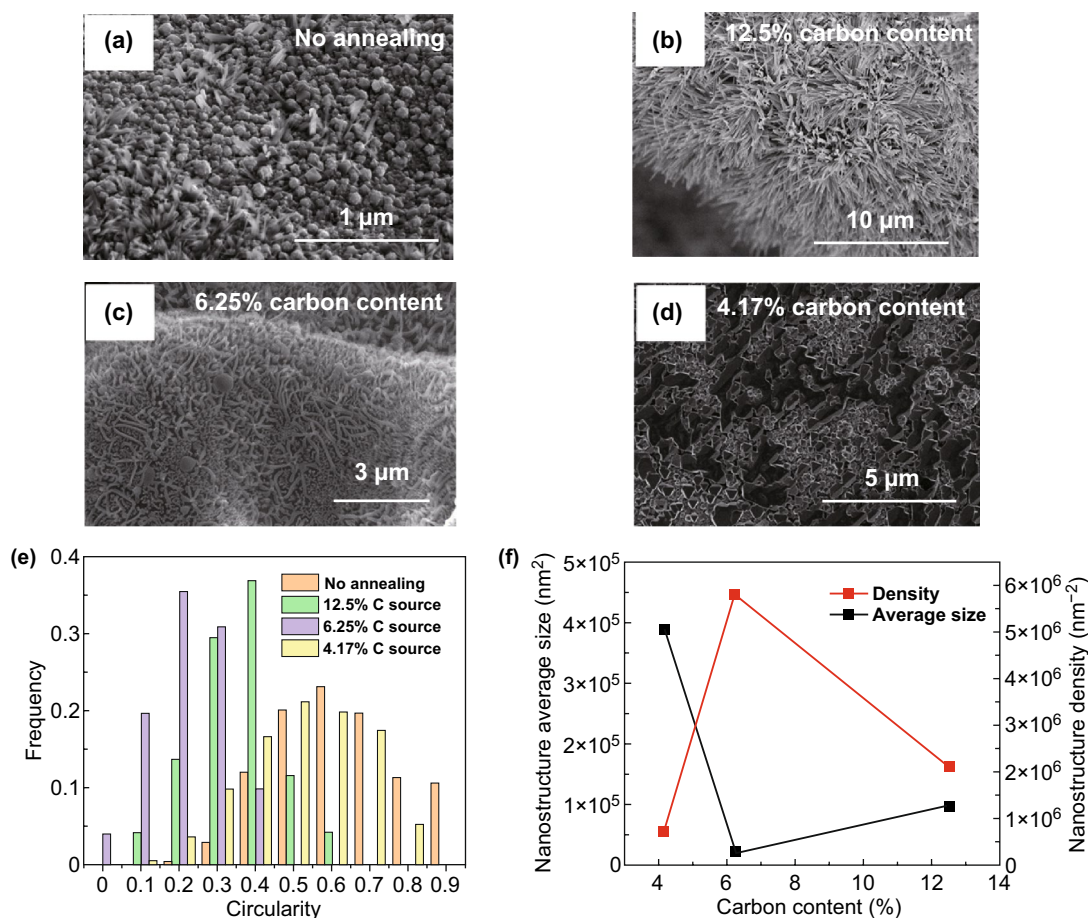


**Fig. 2** **a** Scanning electron microscopy (SEM) image of nanocore  $\text{Ni}_3\text{Si}_2$  nanostructure. **b** SEM image of nanowire  $\text{Ni}_3\text{Si}_2$  nanostructure. **c** SEM image of creeper-like  $\text{Ni}_3\text{Si}_2$  nanostructure. **d** SEM image of amorphous  $\text{Ni}_3\text{Si}_2$  nanostructure. **e** Circularity frequency distribution. **f** Time-dependent variation in the average size and density of creeper-like  $\text{Ni}_3\text{Si}_2/\text{NiOOH}/\text{graphene}$  nanostructures on 3D graphene/Ni foam. The images were obtained at different carbon contents during annealing

can be attributed to the (041), (242), (331), and (201) planes of the  $\text{Ni}_3\text{Si}_2$  structure, respectively [22]. And the lattice fringe distance of 0.70 nm is attributed to the (003) planes of the NiOOH [23, 24]. Figure 4e shows that the creeper-like nanostructures contain uniformly distributed C, Ni, O, and Si.

Raman spectroscopy was conducted to investigate the crystalline structure of the  $\text{Ni}_3\text{Si}_2/\text{NiOOH}/\text{graphene}$  (Fig. 5a). The Raman spectrum of graphene shows two main vibration bands at 1583 and 2696  $\text{cm}^{-1}$ , corresponding to the G and 2D bands of graphene, respectively. Compared with that of the graphene peaks [25], the peaks in Raman spectra of  $\text{Ni}_3\text{Si}_2$  and NiOOH indicate a clearly distinct set of low-intensity vibration modes. The band at 221  $\text{cm}^{-1}$  belongs to  $\text{Ni}_3\text{Si}_2$  and represents the excitation band of a single  $\text{Ni}_3\text{Si}_2$

phase [26]. The bands at 463 and 3578  $\text{cm}^{-1}$  are attributed to NiOOH [27].

Typical XRD patterns of the  $\text{Ni}_3\text{Si}_2/\text{NiOOH}/\text{graphene}$  nanostructure and NiOOH/graphene are shown in Fig. 5b. The high-intensity peak at 26.5° is related to the (002) crystal plane of graphene (JCPDS 23-0064). The diffraction peak at 12.8° corresponds to the (003) plane of NiOOH (JCPDS 06-0075). The characteristic peaks at 23.3°, 33.2°, 44.9°, and 52.8° are attributed to the (310), (330), (242), and (004) crystal planes of  $\text{Ni}_3\text{Si}_2$  (JCPDS No. 017-0881), respectively. Compared with that of NiOOH/graphene, the intensity of the graphene and NiOOH peaks is much stronger than that of  $\text{Ni}_3\text{Si}_2/\text{NiOOH}/\text{graphene}$ , which could be caused by the presence of unrepaired defects such as lattice mismatch.

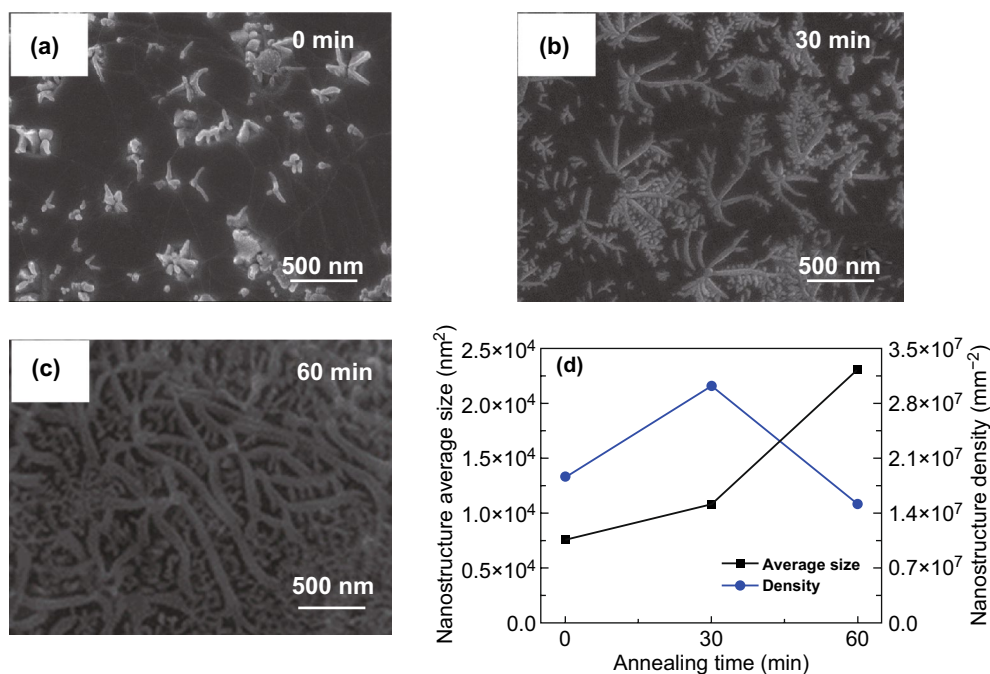


**Fig. 3** SEM images of Ni-Si nanostructures for growth periods **a** of 0 min with 6.25% carbon content, **b** of 30 min with 6.25% carbon content, **c** of 60 min with 6.25% carbon content. **d** Time-dependent variation in the average size and density of nanostructures

The chemical compositions of the Ni<sub>3</sub>Si<sub>2</sub>/NiOOH/graphene materials were characterized via XPS. The survey

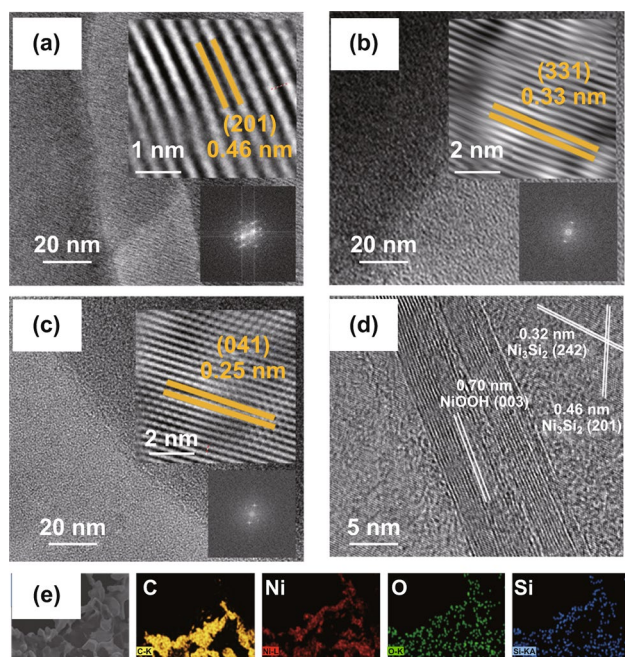


**Fig. 4** **a–d** TEM images of Ni<sub>3</sub>Si<sub>2</sub>/NiOOH/graphene creeper-like nanostructures. **e** EDS scans of Ni<sub>3</sub>Si<sub>2</sub>/NiOOH/graphene creeper-like nanostructures

scan spectra (Fig. 5c–f) exhibit Ni 2p<sub>1/2</sub>, Ni 2p<sub>3/2</sub>, Si 2p, and O 1s peaks. The Ni 2p<sub>1/2</sub> spectrum in Fig. 5c shows two major peaks with binding energies of 870.02 and 874.9 eV, which correspond to Ni<sub>3</sub>Si<sub>2</sub> and NiOOH, respectively. The Ni 2p<sub>3/2</sub> spectrum in Fig. 5d shows a peak at 852.4 eV, which is due to Ni<sub>3</sub>Si<sub>2</sub>. The Si 2p peak at 99.51 eV corresponds to Ni<sub>3</sub>Si<sub>2</sub> (Fig. 5e). The strong peak at 533.6 eV in the O 1s spectrum is due to NiOOH (Fig. 5f).

### 3.2 Electrochemical Characterization

To determine the electrochemical performance of the positive electrode, cyclic voltammetry (CV), galvanostatic charge/discharge (GCD), and electrochemical impedance spectroscopy (EIS) of the Ni<sub>3</sub>Si<sub>2</sub>/NiOOH/graphene were performed in a 3 M KOH solution using a three-electrode system. We combined nanowire-shaped, creeper-shaped and amorphous Ni<sub>3</sub>Si<sub>2</sub>/graphene with NiOOH, respectively, denoted as Ni<sub>3</sub>Si<sub>2</sub>/NiOOH/graphene-1, Ni<sub>3</sub>Si<sub>2</sub>/NiOOH/graphene-2 and Ni<sub>3</sub>Si<sub>2</sub>/NiOOH/graphene-3. From Fig. S5a, the Ni<sub>3</sub>Si<sub>2</sub>/NiOOH/graphene-2 electrodes show considerably largest enclosed areas, which indicates that electrochemical capacitance is improved owing to pseudocapacitive

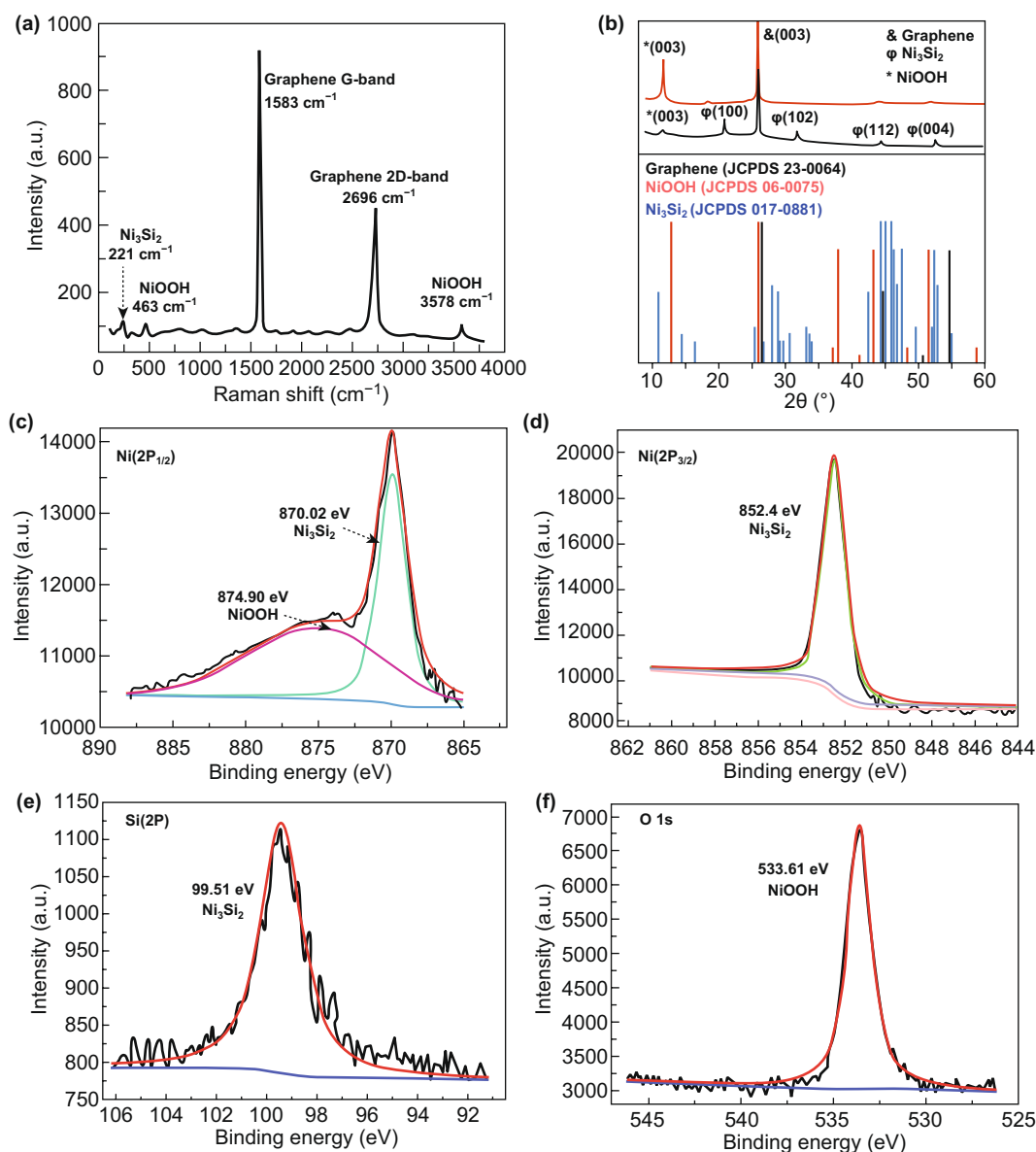


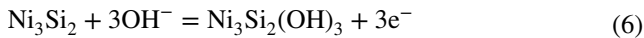
**Fig. 5** **a** Raman spectra of  $\text{Ni}_3\text{Si}_2/\text{NiOOH}/\text{graphene}$ . **b** XRD patterns of  $\text{NiOOH}/\text{graphene}$  and  $\text{Ni}_3\text{Si}_2/\text{NiOOH}/\text{graphene}$ . **c–f** XPS survey spectra of  $\text{Ni}_3\text{Si}_2/\text{NiOOH}/\text{graphene}$  electrodes ( $\text{Ni } 2p$ ,  $\text{Si } 2p$ , and  $\text{O } 1s$ )

contributions. Furthermore, for the GCD measurements (Fig. S5b),  $\text{Ni}_3\text{Si}_2/\text{NiOOH}/\text{graphene}$ -1, -2 and -3 electrodes clearly differ owing to the significant contributions from Faradaic capacitance. The considerably extended discharge time of  $\text{Ni}_3\text{Si}_2/\text{NiOOH}/\text{graphene}$ -2 again proves their enhanced capacitance. The Nyquist plots obtained by EIS are composed of an arc in the high-frequency region and a straight line in the low-frequency region, which can be simulated by an equivalent circuit (Fig. S5c). Obviously,  $\text{Ni}_3\text{Si}_2/\text{NiOOH}/\text{graphene}$ -2 has minimal series ( $0.28 \Omega$ ) and

contact resistances ( $0.8 \Omega$ ), which indicates better capacitance performance. It attributed to creeper-like  $\text{Ni}_3\text{Si}_2/\text{graphene}$  nanostructure has smaller crystal size and higher density. Electrolyte ions fully contact with the electrode and increase the effective specific surface area, and the creeper-like  $\text{Ni}_3\text{Si}_2/\text{NiOOH}/\text{graphene}$  electrode provides more active sites to store energy.

Figure 6a shows the comparison between different CV curves obtained at a scan rate of  $10 \text{ mV s}^{-1}$ . The area of the CV curve of the electrode with  $\text{Ni}_3\text{Si}_2/\text{NiOOH}/\text{graphene}$  is

larger than that of NiOOH/graphene and Ni<sub>3</sub>Si<sub>2</sub>/graphene, which indicates high capacitance. Notably, the three CV curves show different redox peaks at the same scanning rate because the Gibbs free energy of the surface redox reaction of Ni<sub>2p</sub>/Ni<sub>3p</sub> differs. The relative redox process can be described using Eqs. (5) and (6):



With increasing scan rate, the current response increases concomitant with the shift of the redox peaks; thus, the Faradic reaction may be controlled by ion diffusion. The storage mechanisms of the electrodes were studied by analyzing the relationship between the peak current ( $i$ ) and scan rate ( $\nu$ ) using Eqs. (7) and (8):

$$i = a\nu^b \quad (7)$$

$$\log(i) = \log(a) + b \log(\nu) \quad (8)$$

The  $b$  value generated by the slope can be used to determine the control mechanism of the electrode. Typically,  $b$  values close to 1.0 and 0.5 indicate pseudocapacitive behavior

and a battery (diffusion-controlled) process, respectively. As shown in Fig. 6b, the  $b$  values for the anodic peaks in Ni<sub>3</sub>Si<sub>2</sub>/graphene and Ni<sub>3</sub>Si<sub>2</sub>/NiOOH/graphene are 0.69 and 0.59, respectively, indicating that the specific capacitances of the electrodes are based on both diffusion-controlled and pseudocapacitive behaviors. Adding NiOOH increases the size of the nanostructure and proportion of the current generated by the volume response. Therefore, the Ni<sub>3</sub>Si<sub>2</sub>/NiOOH/graphene electrode mainly exhibits diffusion control. The pseudocapacitive contribution can be investigated using the CV curves and Eqs. (9) and (10):

$$i(V) = k_1\nu + k_2\nu^{0.5} \quad (9)$$

$$\frac{i(V)}{\nu^{0.5}} = k_1\nu^{0.5} + k_2 \quad (10)$$

where  $k_1$  and  $k_2$  are changeable parameters originating from the slope and  $y$ -axis intercept of the curves between  $i\nu^{-0.5}$  and  $\nu^{0.5}$ . The parameters  $k_1\nu$  and  $k_2\nu^{0.5}$  represent the fractions of the capacitive and diffusion-controlled behaviors, respectively. The pseudocapacitive contribution fractions are shown in Fig. 6c. Based on the above-mentioned calculation, the pseudocapacitive contributions obtained for Ni<sub>3</sub>Si<sub>2</sub>/graphene are 75.6%, 81.1%, 93.0%, 94.4%, and 95.5% at scan

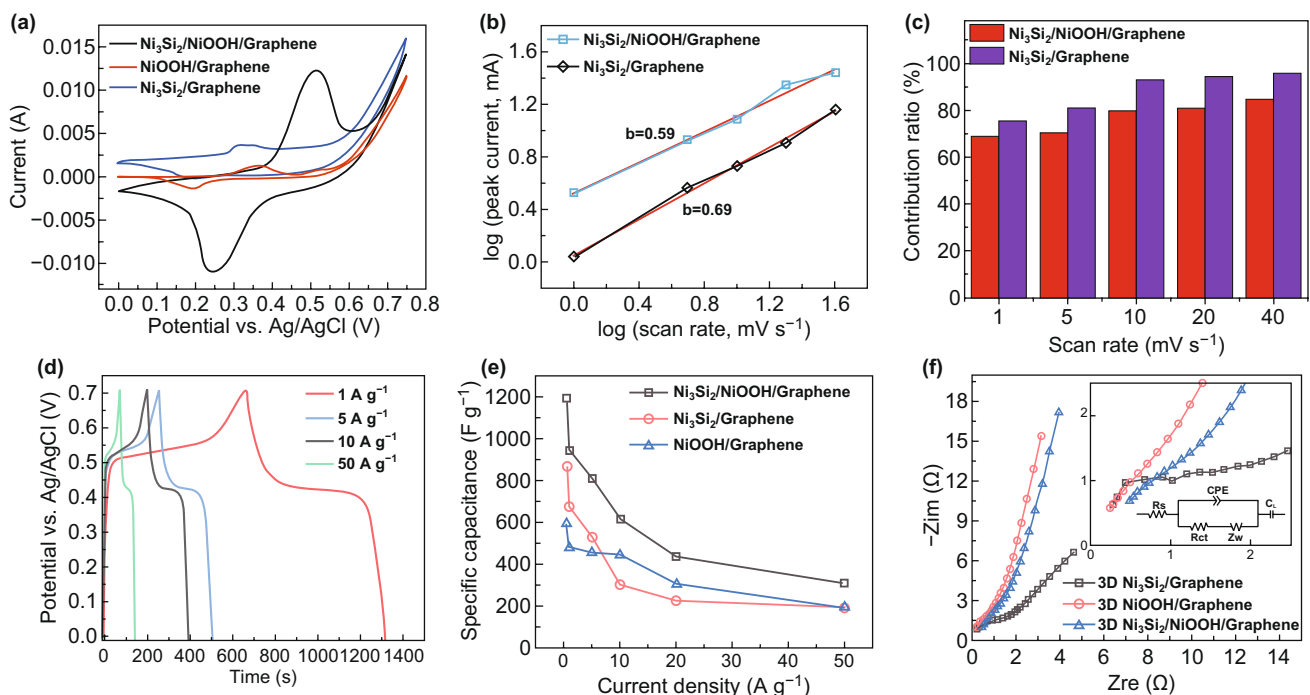


**Fig. 6** **a** Cyclic voltammetry (CV) curves at 10 mV s<sup>-1</sup>. **b** Log (scan rate) versus log (peak current) graph for the anodic peaks. **c** Pseudocapacitive contribution (%) at different scan rates. **d** Galvanostatic charge/discharge (GCD) curves at various current densities. **e** Specific capacitance depending on the current density. **f** Nyquist plots of Ni<sub>3</sub>Si<sub>2</sub>/NiOOH/graphene, Ni<sub>3</sub>Si<sub>2</sub>/graphene, and NiOOH/graphene

rates of 1, 5, 10, 20, and 40  $\text{mV s}^{-1}$ , respectively. Similarly, the ratios of the pseudocapacitive contribution of  $\text{Ni}_3\text{Si}_2/\text{NiOOH}/\text{graphene}$  are 69.1%, 70.3%, 79.8%, 80.8%, and 84.4% at scan rates of 1, 5, 10, 20, and 40  $\text{mV s}^{-1}$ , respectively. At high scan rates, the pseudocapacitive storage behavior is outstanding because fast ion intercalation/deintercalation produces good reversibility and rate capability.

In addition, the GCD curves of  $\text{Ni}_3\text{Si}_2/\text{NiOOH}/\text{graphene}$  are shown in Fig. 6d. The GCD curves show pairs of voltage platforms during the long charge–discharge process, which indicates a superior Faradic efficiency and excellent reversibility. From the plot of Coulombic efficiency (Fig. S3), the Coulomb efficiency is 95.52% at a current density of 1  $\text{A g}^{-1}$ . Even at a high current density of 50  $\text{A g}^{-1}$ , the Coulomb efficiency can reach 86.93%. The specific capacity of the device at a current density of 1  $\text{A g}^{-1}$  calculated from the discharge branch of the device is 835.3  $\text{C g}^{-1}$  (1193.28  $\text{F g}^{-1}$ ). The specific capacitance values of the electrodes were calculated based on their corresponding GCD curves, as shown in Fig. 6e. At the same current density, the performance of the  $\text{Ni}_3\text{Si}_2/\text{NiOOH}/\text{graphene}$  electrode is much better than that of the  $\text{Ni}_3\text{Si}_2/\text{graphene}$ , and  $\text{NiOOH}/\text{graphene}$  electrodes because adding  $\text{NiOOH}$  provides more active sites and accelerates the ion exchange of the electrode surface in alkaline solution. The electrons react with  $\text{NiOOH}$  on the surface to generate  $\text{Ni}(\text{OH})_2$  and  $\text{OH}^-$ . Then,  $\text{OH}^-$  reacts with  $\text{Ni}_3\text{Si}_2$  to generate electrons and  $\text{Ni}_3\text{Si}_2(\text{OH})_3$ . It is a positive feedback process until the electrode material is transformed into  $\text{Ni}(\text{OH})_2$  and  $\text{Ni}_3\text{Si}_2(\text{OH})_3$ . Additionally, the unique spatial structure of  $\text{Ni}_3\text{Si}_2$  eases the agglomeration and deformation of  $\text{NiOOH}$ .

The Nyquist plots of  $\text{Ni}_3\text{Si}_2/\text{graphene}$ ,  $\text{NiOOH}/\text{graphene}$ , and  $\text{Ni}_3\text{Si}_2/\text{NiOOH}/\text{graphene}$  are shown in Fig. 6f. The charge-transfer resistance of the  $\text{NiOOH}/\text{Graphene}$  electrode,  $\text{Ni}_3\text{Si}_2/\text{Graphene}$  electrode, and  $\text{Ni}_3\text{Si}_2/\text{NiOOH}/\text{Graphene}$  electrode are 0.4, 0.97, and 0.36  $\Omega$ , respectively. The equivalent series resistance is 0.23, 0.28, and 0.47  $\Omega$  for the  $\text{NiOOH}/\text{Graphene}$  electrode,  $\text{Ni}_3\text{Si}_2/\text{Graphene}$  electrode, and  $\text{Ni}_3\text{Si}_2/\text{NiOOH}/\text{Graphene}$  electrode, respectively.  $\text{Ni}_3\text{Si}_2/\text{NiOOH}/\text{graphene}$  has the largest equivalent series resistance, which is due to the lattice mismatch at the interface of  $\text{Ni}_3\text{Si}_2$  and  $\text{NiOOH}$ . In an alkaline environment, a protective layer of  $\text{SiO}_2 \cdot 2\text{H}_2\text{O}$  and/or  $\text{Ni}_2\text{SiO}_4$  can form on the surface of  $\text{Ni}_3\text{Si}_2$ . Because  $\text{Ni}_2\text{SiO}_4$  and  $\text{SiO}_2 \cdot 2\text{H}_2\text{O}$  are insulators, the charge transfer and diffusion processes on the electrode surface are suppressed [28]. Therefore,  $\text{Ni}_3\text{Si}_2/\text{graphene}$

has the largest Warburg and charge-transfer resistances.  $\text{NiOOH}$  has excellent conductivity and prevents insulator production on the electrode surface, which considerably reduces difficulties in transporting charges. In the low-frequency region, the slope of the straight line indicates the difficulty of ion diffusion. The closer the angle between the line and the  $x$ -axis is to  $90^\circ$ , the higher the transmission efficiency of surface ions. The angle of the  $\text{NiOOH}/\text{Graphene}$  electrode,  $\text{Ni}_3\text{Si}_2/\text{Graphene}$  electrode, and  $\text{Ni}_3\text{Si}_2/\text{NiOOH}/\text{Graphene}$  electrode are  $83.48^\circ$ ,  $60.53^\circ$ , and  $79.70^\circ$ . Overall,  $\text{Ni}_3\text{Si}_2/\text{NiOOH}/\text{graphene}$  has faster kinetics, higher conductivity, and a lower ion diffusion resistance during the charge–discharge process.

### 3.3 $\text{Ni}_3\text{Si}_2/\text{NiOOH}/\text{graphene}$ Symmetric Supercapacitors

$\text{Ni}_3\text{Si}_2/\text{NiOOH}/\text{graphene}$  was chosen to assemble symmetrical all-solid-state SCs and explore their energy storage performances. Figure 7a displays the CV curves of an all-solid-state SC at different scan rates and a voltage window ranging from 0 to 1.0 V. The volt–ampere cycle curve is rectangular and shows a wide peak. Electrolyte ions undergo a rapid and highly reversible process of insertion and removal on the electrode surface, which represents the mechanism of ion intercalation in a Faraday quasi-capacitor. Figure 7b outlines the charge–discharge storage capacity of the devices based on the GCD at different current densities. The shape of the GCD curve is symmetrical and a charge–discharge platform appears during the charge–discharge process, indicating that the device exhibits pseudocapacitive behavior. The specific capacities are 186.5 (186.5  $\text{F g}^{-1}$ ), 126.3, 71.4, and 58.5  $\text{C g}^{-1}$  at 0.3, 0.6, 1.2, and 3  $\text{mA cm}^{-2}$ , respectively. Figure 7c shows the Nyquist plots of the all-solid-state SCs. The equivalent series resistance of the capacitors is  $\sim 0.1 \Omega$  and the charge-transfer resistance is  $\sim 0.5 \Omega$ . The large slope in the low-frequency region indicates that the Warburg impedance is minimal. The energy and power densities of the all-solid-state SC were calculated according to the discharged branches of the GCD curves (Fig. 7d). The maximal energy density is 25.9  $\text{Wh kg}^{-1}$  at 750  $\text{W kg}^{-1}$ , and the maximal power density is 7500  $\text{W kg}^{-1}$  at 8.13  $\text{Wh kg}^{-1}$ . Compared with previous reports [29–33], the  $\text{Ni}_3\text{Si}_2/\text{NiOOH}/\text{graphene}$  all-solid-state SC exhibits higher energy and power densities.

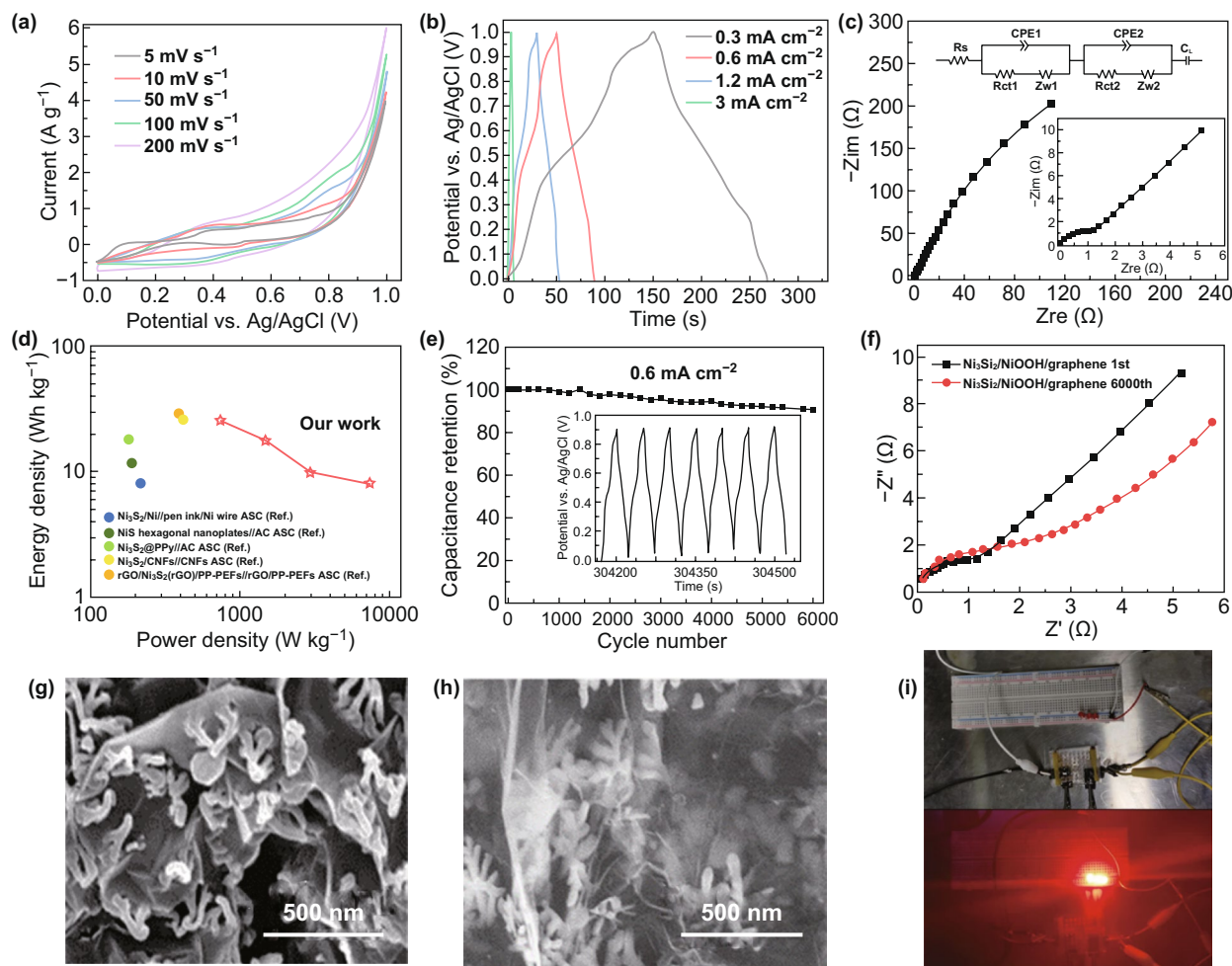


**Fig. 7** **a** CV curves of the all-solid-state  $\text{Ni}_3\text{Si}_2/\text{NiOOH}/\text{graphene}$  supercapacitor (SC). **b** GCD curves of the all-solid-state  $\text{Ni}_3\text{Si}_2/\text{NiOOH}/\text{graphene}$  SC. **c** Nyquist plots of the all-solid-state  $\text{Ni}_3\text{Si}_2/\text{NiOOH}/\text{graphene}$  SC. **d** Ragone plot of the all-solid-state  $\text{Ni}_3\text{Si}_2/\text{NiOOH}/\text{graphene}$  SC. **e** Cyclic lifetime of the all-solid-state  $\text{Ni}_3\text{Si}_2/\text{NiOOH}/\text{graphene}$  SC. **f** Nyquist plot of the  $\text{Ni}_3\text{Si}_2/\text{NiOOH}/\text{graphene}$  electrode before and after 6000 cycling. **g** SEM images of the  $\text{Ni}_3\text{Si}_2/\text{NiOOH}/\text{graphene}$  electrode before cycling. **h** SEM images of the  $\text{Ni}_3\text{Si}_2/\text{NiOOH}/\text{graphene}$  electrode after 6000 cycling at  $0.6 \text{ mA cm}^{-2}$ . **i** Device connection diagram and the device to light up a LED light

Therefore, the  $\text{Ni}_3\text{Si}_2/\text{NiOOH}/\text{graphene}$  all-solid-state SC can store more energy per unit weight and output a larger current density. Figure 7e shows the cyclic stability of all-solid-state capacitors. At a current density of  $0.6 \text{ mA cm}^{-2}$ , 90.7% of the capacitance is maintained after 6000 cycles. From Fig. 7g, h, after 6000 charge and discharge cycles, the  $\text{Ni}_3\text{Si}_2$  structure has not changed significantly, it demonstrates the durability of the  $\text{Ni}_3\text{Si}_2/\text{NiOOH}/\text{graphene}$  nanostructure. But a thin film is formed on the surface of the electrode to wrap the entire electrode. Figure 7f shows that due to the existence of the thin film, the contact resistance and Warburg resistance of the electrode increase. It

indicated that the thin film reduces the active sites on the electrode surface and reduces the electrolyte ion exchange efficiency. In Fig. 7i, we connected two  $\text{Ni}_3\text{Si}_2/\text{NiOOH}/\text{graphene}$  supercapacitors in series and charge the supercapacitor system to 2 V. When the voltage across the system reaches 2 V, disconnect the charging system and drive the LED light. In addition,  $\text{Ni}_3\text{Si}_2/\text{NiOOH}/\text{graphene}$  demonstrates superior specific capacitance by comparison with other materials (Table 1). Generally, the  $\text{Ni}_3\text{Si}_2/\text{NiOOH}/\text{graphene}$  all-solid-state SC has impressive storage and output capabilities and can be applied in applications such as integrated circuits.

**Table 1** Electrochemical properties of different nickel compounds and silicides and their composites as electrode materials

Electrode materials	Electrolyte	Specific capacitance (F g <sup>-1</sup> )	Cycle	Energy density (Wh kg <sup>-1</sup> )	Refs.
NiOOH-decorated $\alpha$ -FeOOH	1 M KOH	554.17 (at 1.1 A g <sup>-1</sup> )	82.61% (4000 cycles)	–	[34]
Ni(OH) <sub>2</sub> /NG	6 M KOH	1350 (at 2 A g <sup>-1</sup> )	83.08% (1000 cycles)	–	[35]
Ni/GO	6 M KOH	461 (at 5 mV s <sup>-1</sup> )	98.05% (1000 cycles)	–	[36]
H-NiOOH/GS	2 M KOH	1162 (at 1 A g <sup>-1</sup> )	85.3% (8000 cycles)	66.8 (800 W kg <sup>-1</sup> )	[37]
CoNiSi/C	3 M KOH	226 (at 0.5 A g <sup>-1</sup> )	99% (10,000 cycles)	20 (94.5 W kg <sup>-1</sup> )	[38]
NiSi hollow sphere	3 M KOH	66.7 (at 0.5 A g <sup>-1</sup> )	44% (5000 cycles)	3.78	[39]
NiSi–Ni(OH) <sub>2</sub>	3 M KOH	476.4 (at 2 A g <sup>-1</sup> )	103% (10,000 cycles)	21.6 (413.7 W kg <sup>-1</sup> )	[40]
Nickel silicide nanowires	2 M KOH	187.92 (at 2 A g <sup>-1</sup> )	79% (3000 cycles)	13.37 (200 W kg <sup>-1</sup> )	[41]
Ni <sub>3</sub> Si <sub>2</sub> nanowires	2 M KOH	760 (at 0.5 A g <sup>-1</sup> )	60% (1000 cycles)	17.5 (301 W kg <sup>-1</sup> )	[7]
Ni <sub>3</sub> Si <sub>2</sub> /NiOOH/graphene	3 M KOH	1193.28 (at 1 A g <sup>-1</sup> )	90.7% (6000 cycles)	25.9 (750 W kg <sup>-1</sup> )	Our work

## 4 Conclusions

In summary, we successfully fabricated novel creeper-like Ni<sub>3</sub>Si<sub>2</sub>/graphene nanostructures using LSRCVD based on which Ni<sub>3</sub>Si<sub>2</sub>/NiOOH/graphene nanostructures were hydrothermally synthesized. Based on the SEM images, the Ni<sub>3</sub>Si<sub>2</sub>/graphene nanostructures formed in a carbon-rich atmosphere by melting the surface of Ni foam and condensing the resulting vapor, by growth of 3D graphene by Ni, and by nucleation of Ni–Si. By adjusting the growth temperature and duration, the nucleation and evolution of these creeper-like nanostructures can be precisely controlled. The electrochemical measurement results show that creeper-like Ni<sub>3</sub>Si<sub>2</sub>/NiOOH/graphene nanostructures exhibit excellent performances and are suitable for use as energy storage materials. The charge storage mechanism of Ni<sub>3</sub>Si<sub>2</sub>/NiOOH/graphene used as SC electrode is primarily determined by two types of Ni<sub>2p</sub>/Ni<sub>3p</sub> pseudocapacitive reactions. Creeper-like nanostructured electrodes provide a high specific capacitance (1193.28 F g<sup>-1</sup> at 1 A g<sup>-1</sup>). The all-solid-state SCs based on Ni<sub>3</sub>Si<sub>2</sub>/NiOOH/graphene nanostructures exhibit outstanding supercapacitor performance, exhibiting an extremely high-energy density (25.9 Wh kg<sup>-1</sup> at 750 W kg<sup>-1</sup>). Even after 6000 cycles at 0.6 mA cm<sup>-2</sup>, only 10% of the capacitance is lost. This impressive electrochemical behavior indicates that creeper-like Ni<sub>3</sub>Si<sub>2</sub>/NiOOH/graphene nanostructures have great potential in the energy storage field.

**Acknowledgements** The work was supported by the Natural Science Basic Research Plan in Shaanxi Province of China (Program Nos. 2019ZDLGY16-02, 2019ZDLGY16-03, and 2019ZDLGY16-08); Youth Science and Technology Nova Program of Shaanxi

Province (2020KJXX-068); the Wuhu and Xidian University special fund for industry-university-research cooperation (Program No.HX01201909039).

**Open Access** This article is licensed under a Creative Commons Attribution 4.0 International License, which permits use, sharing, adaptation, distribution and reproduction in any medium or format, as long as you give appropriate credit to the original author(s) and the source, provide a link to the Creative Commons licence, and indicate if changes were made. The images or other third party material in this article are included in the article's Creative Commons licence, unless indicated otherwise in a credit line to the material. If material is not included in the article's Creative Commons licence and your intended use is not permitted by statutory regulation or exceeds the permitted use, you will need to obtain permission directly from the copyright holder. To view a copy of this licence, visit <http://creativecommons.org/licenses/by/4.0/>.

**Electronic supplementary material** The online version of this article (<https://doi.org/10.1007/s40820-020-00527-w>) contains supplementary material, which is available to authorized users.

## References

1. M. Fan, B. Ren, L. Yu, Q. Liu, J. Wang et al., Facile growth of hollow porous NiO microspheres assembled from nanosheet building blocks and their high performance as a supercapacitor electrode. *Cryst. Eng. Commun.* **16**, 10389–10394 (2014). <https://doi.org/10.1039/C4CE01242A>
2. Y. Yang, Z. Hu, Z. Zhang, F. Zhang, Y. Zhang et al., Reduced graphene oxide–nickel oxide composites with high electrochemical capacitive performance. *Mater. Chem. Phys.* **133**, 363–368 (2012). <https://doi.org/10.1016/j.matchemphys.2012.01.039>
3. S. Pilban Jahromi, A. Pandikumar, B.T. Goh, Y.S. Lim, W.J. Basirun, H.N. Lim, N.M. Huang, Influence of particle size on performance of a nickel oxide nanoparticle-based

- supercapacitor. *RSC Adv.* **5**, 14010–14019 (2015). <https://doi.org/10.1039/C4RA16776G>
4. G. Nagaraju, R. Kakarla, S. Cha, J. Yu, Highly flexible conductive fabrics with hierarchically nanostructured amorphous nickel tungsten tetraoxide for enhanced electrochemical energy storage. *Nano Res.* **8**, 3749–3763 (2015). <https://doi.org/10.1007/s12274-015-0874-z>
  5. H. Chen, Y. Lin, Y. Chen, C. Chen, Facile fabrication of three-dimensional hierarchical nanoarchitectures of VO<sub>2</sub>/graphene@NiS<sub>2</sub> hybrid aerogel for high-performance all-solid-state asymmetric supercapacitors with ultrahigh energy density. *ACS Appl. Energy Mater.* **2**, 459–467 (2019). <https://doi.org/10.1021/acsaem.8b01486>
  6. P. Wu, D. Wang, J. Ning, J. Zhang, X. Feng, J. Dong, Y. Hao, Novel 3D porous graphene/Ni<sub>3</sub>S<sub>2</sub> nanostructures for high-performance supercapacitor electrodes. *J. Alloys Compd.* **731**, 1063–1068 (2017). <https://doi.org/10.1016/j.jallcom.2017.10.060>
  7. Y. Jiang, Z. Li, B. Li, J. Zhang, C. Niu, Ni<sub>3</sub>Si<sub>2</sub> nanowires grown in situ on Ni foam for high-performance supercapacitors. *J. Power Sources* **320**, 13–19 (2016). <https://doi.org/10.1016/j.jpowsour.2016.04.077>
  8. J. Ning, D. Wang, J. Zhang, X. Feng, R. Zhong et al., One-step synthesis of novel snowflake-like Si–O/Si–C nanostructures on 3D graphene/Cu foam by chemical vapor deposition. *Nano Res.* **11**, 1861–1872 (2018). <https://doi.org/10.1007/s12274-017-1804-z>
  9. G. Yilmaz, X. Lu, G. Ho, Cross-linker mediated formation of sulfur-functionalized V<sub>2</sub>O<sub>5</sub>/graphene aerogels and their enhanced pseudocapacitive performance. *Nanoscale* **9**, 802–811 (2017). <https://doi.org/10.1039/C6NR08233E>
  10. J. Hu, T.W. Odom, C.M. Lieber, Chemistry and physics in one-dimension: synthesis and properties of nanowires and nanotubes. *Acc. Chem. Res.* **32**, 435–445 (1999). <https://doi.org/10.1021/ar9700365>
  11. Z. Wang, Characterizing the structure and properties of individual wire-like nanoentities. *Adv. Mater.* **12**, 1295–1298 (2000). [https://doi.org/10.1002/1521-4095\(200009\)12:17%3c1295:AID-ADMA1295%3e3.0.CO;2-B](https://doi.org/10.1002/1521-4095(200009)12:17%3c1295:AID-ADMA1295%3e3.0.CO;2-B)
  12. X. Yan, X. Tong, L. Ma, Y. Tian, Y. Cai et al., Synthesis of porous NiS nanoflake arrays by ion exchange reaction from NiO and their high performance supercapacitor properties. *Mater. Lett.* **124**, 133–136 (2014). <https://doi.org/10.1016/j.matlet.2014.03.067>
  13. Y. Chang, Y. Sui, J. Qi, L. Jiang, Y. He et al., Facile synthesis of Ni<sub>3</sub>S<sub>2</sub> and Co<sub>9</sub>S<sub>8</sub> double-size nanoparticles decorated on rGO for high-performance supercapacitor electrode materials. *Electrochim. Acta* **226**, 69–78 (2017). <https://doi.org/10.1016/j.electacta.2016.12.184>
  14. C. Dai, P. Chien, J. Lin, S. Chou, W. Wu et al., Hierarchically structured Ni<sub>3</sub>S<sub>2</sub>/carbon nanotube composites as high performance cathode materials for asymmetric supercapacitors. *ACS Appl. Mater. Interfaces* **5**, 12168–12174 (2013). <https://doi.org/10.1021/am404196s>
  15. J. Wang, D. Chao, J. Liu, L. Li, L. Lai, J. Lin, Z. Shen, Ni<sub>3</sub>S<sub>2</sub>@MoS<sub>2</sub> core/shell nanorod arrays on Ni foam for high-performance electrochemical energy storage. *Nano Energy* **7**, 151–160 (2014). <https://doi.org/10.1016/j.nanoen.2014.04.019>
  16. H. Pang, C. Wei, X. Li, G. Li, Y. Ma et al., Microwave-assisted synthesis of NiS<sub>2</sub> nanostructures for supercapacitors and cocatalytic enhancing photocatalytic H<sub>2</sub> production. *Sci. Rep.* **4**, 3577 (2014). <https://doi.org/10.1038/srep03577>
  17. K. Krishnamoorthy, G. Veerasubramani, S. Radhakrishnan, S. Kim, One pot hydrothermal growth of hierarchical nanostructured Ni<sub>3</sub>S<sub>2</sub> on Ni foam for supercapacitor application. *Chem. Eng. J.* **251**, 116–122 (2014). <https://doi.org/10.1016/j.cej.2014.04.006>
  18. E. Kamali-Heidari, Z. Xu, M. Sohi, A. Ataie, J. Kim, Core-shell structured Ni<sub>3</sub>S<sub>2</sub> nanorods grown on interconnected Ni-graphene foam for symmetric supercapacitors. *Electrochim. Acta* **271**, 507–518 (2018). <https://doi.org/10.1016/j.electacta.2018.03.183>
  19. J. He, C. Guo, S. Zhou, Y. Zhao, Q. Wang et al., Dual carbon-modified nickel sulfide composites toward high-performance electrodes for supercapacitors. *Inorg. Chem. Front.* **6**, 226–232 (2019). <https://doi.org/10.1039/C8QI01024B>
  20. L. Wang, J. Wang, F. Guo, L. Ma, Y. Ren et al., Understanding the initial irreversibility of metal sulfides for sodium-ion batteries, via operando, techniques. *Nano Energy* **43**, 184–191 (2018). <https://doi.org/10.1016/j.nanoen.2017.11.029>
  21. Y. Wu, J. Xiang, C. Yang, W. Lu, C. Lieber, Single-crystal metallic nanowires and metal/semiconductor nanowire heterostructures. *Nature* **430**, 61–65 (2004). <https://doi.org/10.1038/nature02674>
  22. X. Fan, H. Zhang, N. Du, D. Yang, Phase-controlled synthesis of nickel silicide nanostructures. *Mater. Res. Bull.* **47**, 3797–3803 (2012). <https://doi.org/10.1016/j.materresbull.2012.06.017>
  23. R. Salunkhe, Y. Kaneti, Y. Yamauchi, Metal–organic framework-derived nanoporous metal oxides toward supercapacitor applications: progress and prospects. *ACS Nano* **11**(6), 5293–5308 (2017). <https://doi.org/10.1021/acsnano.7b02796>
  24. S. Liu, S. Lee, U. Patil, I. Shackery, S. Kang, K. Zhang, S. Jun, Hierarchical MnCo-layered double hydroxides@Ni(OH)<sub>2</sub> core–shell heterostructures as advanced electrodes for supercapacitors. *J. Mater. Chem. A* **5**(3), 1043–1049 (2017). <https://doi.org/10.1039/c6ta07842g>
  25. J. Ning, D. Wang, J. Zhang, L. Guo, Y. Hao, Investigation of dielectric substrates on electrical and optical performance of wafer-scale graphene using non-contact methods. *Semicond. Sci. Technol.* **32**, 105001 (2017). <https://doi.org/10.1088/1361-6641/aa832f>
  26. F. Li, H. Yue, P. Wang, Z. Yang, D. Wang et al., Synthesis of core–shell architectures of silicon coated on controllable grown Ni-silicide nanostructures and their lithium-ion battery application. *Cryst. Eng. Commun.* **15**, 7298–7306 (2013). <https://doi.org/10.1039/c3ce40651b>
  27. X. Feng, J. Ning, D. Wang, J. Zhang, J. Dong et al., All-solid-state planar micro-supercapacitor based on graphene/NiOOH/Ni(OH)<sub>2</sub> via mask-free patterning strategy. *J. Power*



- Sources **418**, 130–137 (2019). <https://doi.org/10.1016/j.jpowsour.2019.01.093>
28. P. Nikolaychuk, J. Siberian, Thermodynamic evaluation of electrochemical stability of Me–Si systems (Me = 4th row transition metal). *Fed. Univ. Chem.* **2**, 160–180 (2015). <https://doi.org/10.17516/1998-2836-2015-8-2-160-180>
  29. L. Long, Y. Yao, M. Yan, H. Wang, G. Zhang et al., Ni<sub>3</sub>S<sub>2</sub>@ polypyrrole composite supported on nickel foam with improved rate capability and cycling durability for asymmetric supercapacitor device applications. *J. Mater. Sci.* **52**, 3642–3656 (2017). <https://doi.org/10.1007/s10853-016-0529-9>
  30. Z. Li, X. Yu, A. Gu, H. Tang, L. Wang, Z. Lou, Anion exchange strategy to synthesis of porous NiS hexagonal nanoplates for supercapacitors. *Nanotechnology* **28**, 065406 (2017). <https://doi.org/10.1088/1361-6528/28/6/065406>
  31. W. Yu, W. Lin, X. Shao, Z. Hu, R. Li, D. Yuan, High performance supercapacitor based on Ni<sub>3</sub>S<sub>2</sub>/carbon nanofibers and carbon nanofibers electrodes derived from bacterial cellulose. *J. Power Sources* **272**, 137–143 (2014). <https://doi.org/10.1016/j.jpowsour.2014.08.064>
  32. J. Wen, S. Li, K. Zhou, Z. Song, B. Li et al., Flexible coaxial-type fiber solid-state asymmetrical supercapacitor based on Ni<sub>3</sub>S<sub>2</sub> nanorod array and pen ink electrodes. *J. Power Sources* **324**, 325–333 (2016). <https://doi.org/10.1016/j.jpowsour.2016.05.087>
  33. N. Wang, G. Han, Y. Chang, W. Hou, Y. Xiao, H. Li, Preparing Ni<sub>3</sub>S<sub>2</sub> composite with neural network-like structure for high-performance flexible asymmetric supercapacitors. *Electrochim. Acta* **317**, 322–332 (2019). <https://doi.org/10.1016/j.electacta.2019.06.012>
  34. D. Zhang, X. Kong, M. Jiang, D. Lei, X. Lei, NiOOH-decorated  $\alpha$ -FeOOH nanosheet array on stainless steel for applications in oxygen evolution reactions and supercapacitors. *ACS Sustain. Chem. Eng.* **7**, 4420–4428 (2019). <https://doi.org/10.1016/j.ccej.2019.121938>
  35. D. Pan, M. Zhang, Y. Wang, Z. Yan, J. Jing, J. Xie, In situ fabrication of nickel based oxide on nitrogen-doped graphene for high electrochemical performance supercapacitors. *Chem. Phys. Lett.* **685**, 457 (2017). <https://doi.org/10.1016/j.cplett.2017.08.021>
  36. M. Gopiraman, S. Saravanamoorthy, D. Deng, A. Ilangoan, I. Kim, I. Chung, Facile mechanochemical synthesis of nickel/graphene oxide nanocomposites with unique and tunable morphology: applications in heterogeneous catalysis and supercapacitors. *Catalysts* **9**, 486 (2019). <https://doi.org/10.3390/catal9050486>
  37. R. Wang, C. Xu, J. Lee, High performance asymmetric supercapacitors: new NiOOH nanosheet/graphene hydrogels and pure graphene hydrogels. *Nano Energy* **19**, 210–221 (2016). <https://doi.org/10.1016/j.nanoen.2015.10.030>
  38. Y. Zhang, C. Wang, H. Jiang, Q. Wang, J. Zheng, C. Meng, Cobalt–nickel silicate hydroxide on amorphous carbon derived from bamboo leaves for hybrid supercapacitors. *Chem. Eng. J.* **375**, 121938 (2019). <https://doi.org/10.1016/j.ccej.2019.121938>
  39. Q. Wang, Y. Zhang, J. Xiao, H. Jiang, X. Li, C. Meng, Novel ordered hollow spherical nickel silicate–nickel hydroxide united composite with two types of morphologies for enhanced electrochemical storage performance. *Mater. Chem. Front.* **3**, 2090–2101 (2019). <https://doi.org/10.1039/c9qm00392d>
  40. Q. Wang, Y. Zhang, H. Jiang, X. Li, Y. Cheng, C. Meng, Designed mesoporous hollow sphere architecture metal (Mn Co, Ni) silicate: a potential electrode material for flexible all solid-state asymmetric supercapacitor. *Chem. Eng. J.* **362**, 818–829 (2019). <https://doi.org/10.1016/j.ccej.2019.01.102>
  41. M.M. Ramly, F.S. Omar, A. Rohaizad, Z. Aspanut, S.A. Rahman, B.T. Goh, Solid-phase diffusion controlled growth of nickel silicide nanowires for supercapacitor electrode. *Appl. Surf. Sci.* **456**, 515–525 (2018). <https://doi.org/10.1016/j.apsusc.2018.06.140>